

# Independent tuning of work function and field enhancement factor in hybrid lanthanum hexaboride-graphene-silicon field emitters

Fatemeh Rezaeifar, Qingfeng Lin, Xiangyu Chen, Tracy M. Mattox, Ayush Garg, Andrew Clough, Nirakar Poudel, Louis Blankemeier, Debarghya Sarkar, Stephen B. Cronin, and Rehan Kapadia

Citation: *Journal of Vacuum Science & Technology B, Nanotechnology and Microelectronics: Materials, Processing, Measurement, and Phenomena* **35**, 062202 (2017);

View online: <https://doi.org/10.1116/1.5001324>

View Table of Contents: <http://avs.scitation.org/toc/jvb/35/6>

Published by the [American Vacuum Society](#)

---

---



## Instruments for Advanced Science

Contact Hiden Analytical for further details:

**W** [www.HidenAnalytical.com](http://www.HidenAnalytical.com)

**E** [info@hiden.co.uk](mailto:info@hiden.co.uk)

**CLICK TO VIEW** our product catalogue



### Gas Analysis

- › dynamic measurement of reaction gas streams
- › catalysis and thermal analysis
- › molecular beam studies
- › dissolved species probes
- › fermentation, environmental and ecological studies



### Surface Science

- › UHV TPD
- › SIMS
- › end point detection in ion beam etch
- › elemental imaging - surface mapping



### Plasma Diagnostics

- › plasma source characterization
- › etch and deposition process reaction
- › kinetic studies
- › analysis of neutral and radical species



### Vacuum Analysis

- › partial pressure measurement and control of process gases
- › reactive sputter process control
- › vacuum diagnostics
- › vacuum coating process monitoring

# Independent tuning of work function and field enhancement factor in hybrid lanthanum hexaboride-graphene-silicon field emitters

Fatemeh Rezaeifar and Qingfeng Lin

*Department of Electrical Engineering, University of Southern California, Los Angeles, California 90089*

Xiangyu Chen

*Department of Chemical Engineering and Material Science, University of Southern California, Los Angeles, California 90089*

Tracy M. Mattox

*Molecular Foundry, Lawrence Berkeley National Laboratory, One Cyclotron Road, Berkeley, California 94720*

Ayush Garg

*Department of Electrical Engineering, University of Southern California, Los Angeles, California 90089*

Andrew Clough

*Department of Chemistry and Center for Electron Microscopy and Microanalysis, University of Southern California, Los Angeles, California 90089*

Nirakar Poudel, Louis Blankemeier, Debarghya Sarkar, Stephen B. Cronin, and Rehan Kapadia<sup>a)</sup>

*Department of Electrical Engineering, University of Southern California, Los Angeles, California 90089*

(Received 23 August 2017; accepted 30 October 2017; published 22 November 2017)

The authors report the experimental demonstration of independent control over work function and field enhancement factor in hybrid field emitters using a lanthanum hexaboride (LaB<sub>6</sub>) nanoparticle low-work function coating on monolayer graphene on microfabricated silicon arrays. A critical challenge in field emitters is combining the scalability and uniformity of silicon microfabrication with low-work function materials. Specifically, the authors engineer the field enhancement through microfabrication of the underlying silicon wafers and control the work function by the transfer and deposition of monolayer graphene and LaB<sub>6</sub> nanoparticles. Using this coating, the turn-on electric field, defined as the electric field required for 10  $\mu\text{A}/\text{cm}^2$  of emission current density, drops by  $5\times$  from 12.5 to 2.6 V/ $\mu\text{m}$ . To further analyze these results, the authors carried out detailed electronic and structural characterization of the hybrid emitters to experimentally determine the work function and model the field enhancement factor of the physical structure. Using these coupled simulations and experiments, the authors show that the work function and field enhancement factor can be independently controlled, potentially enabling ultralow turn on, uniform, and stable emitters. *Published by the AVS.* <https://doi.org/10.1116/1.5001324>

## I. INTRODUCTION

Electron emission devices are used in an array of devices such as x-ray tubes,<sup>1</sup> electron beam nanolithography,<sup>2</sup> free electron lasers,<sup>3</sup> flat panel displays,<sup>4</sup> neutron generation,<sup>5,6</sup> scanning tunneling microscopy,<sup>7,8</sup> and vacuum electronic high power terahertz sources.<sup>9</sup> However, due to the large potential barrier to emission of electrons into the vacuum, high fields,<sup>10</sup> temperatures,<sup>11</sup> or high energy photons<sup>12</sup> are typically required to enable useful vacuum emission current levels. During the field emission process, specifically, electrons tunnel through a potential barrier and escape into vacuum. However, to enable significant field emission current, high surface electric fields are needed to thin the tunneling barrier for electrons at the material Fermi level. Thus, reducing the necessary voltage for a given emission current density is a critical challenge for field electron emitters. This challenge is commonly achieved by either using a low work function emitter or sharp features to increase the field

enhancement factor, increasing the local electric field for a given applied field. Carbon-based materials such as carbon nanotubes<sup>13–15</sup> are promising candidates for field emitters, but they suffer from uniformity challenges due to the growth methods. This often leads to only a small fraction of the field emitter arrays tips to be active at a given voltage and often leads to burnout of those emitting tips when the voltage is increased. This challenge has been one of the most significant impediments to widespread adoption of carbon-based field emitters. Graphene is another promising carbon based alternative; however, field emission current from flat sheets of graphene is often small because it is primarily limited to electron emission from the sharp edges of the graphene sheets, which have a lower work function<sup>16,17</sup> and have some field enhancement. However, this limits the area of emission and is challenging to control. With the advances in nanofabrication in recent years, numerous reports have been published on the fabrication and characterization of sharp field emitting tips and nanowire emitter arrays.<sup>18–20</sup> While these approaches offer control over the field enhancement factor, the surface work function is limited by the choice of

<sup>a)</sup>Electronic mail: rkapadia@usc.edu

the nanowire material. Thus, the growth of low-work function nanowire materials such as lanthanum hexaboride ( $\text{LaB}_6$ ) is an active field of research. Arrays of these nanowires suffer from similar uniformity challenges faced by carbon nanotube emitter arrays. By leveraging the well-established silicon microfabrication technology, silicon emitter arrays are significantly more uniform than similar structures created from nanowire or nanotube growth techniques. However, N-type silicon emits electrons with energy  $\sim 4.1$  eV from the vacuum level, and thus still requires relatively high turn on fields. Combining low-work function materials with the uniformity of silicon processing offers the potential to make large area, uniform, low-work function emitters.

Negative electron affinity photocathodes are an important class of emitters under extensive research. By adding a cesium based coating to the surface, a negative electron affinity is achieved. However, these photocathodes are extremely sensitive to contamination on the surface; thus, their preparation, handling, and activation must be performed under ultra-high vacuum of around  $10^{-11}$  Torr.<sup>21</sup> In this paper, the authors intended to introduce a relatively simple fabrication process and demonstrate that by combining graphene with low-work function and long lifetime<sup>22,23</sup>  $\text{LaB}_6$  nanoparticles on arrays of microfabricated silicon tips, we can obtain low-voltage emitters on silicon by reducing the work function of the surface while maintaining the underlying field enhancement of the microfabricated structure. We show experimentally that this reduction in the work function improves the device emission properties by significantly reducing the threshold field and enabling higher current density. To decouple the field enhancement factor and work function, we carry out photoemission spectroscopy (PES) measurements to measure the work function of our emitters, which allows independent extraction of the field enhancement factor from Fowler–Nordheim (FN) analysis of the I-E curves. In addition, using finite element modeling,<sup>24</sup> we investigate the

geometrical field enhancement of the silicon tip array to get an insight into experimental results. We find that the experimental enhancement of local fields between the planar and tip array samples matches well with our simulations. This then enables us to project performance for other geometries of electron emitters using this general approach.

## II. FABRICATION PROCESS

The silicon tip array structure was fabricated on (1 0 0)-oriented, heavily doped *n*-type 2-in. silicon wafers. This wafer size was chosen to ensure that there were no field emission effects from wafer edges and that all the measured emission current occurs from microfabricated silicon tips. The fabrication procedure is summarized in Fig. 1. After removing the native oxide using buffered oxide etch 7:1, LOR 5A was spin coated with 500 rpm for 5 s and 3000 rpm for 60 s and baked at 175 °C for 5 min. Next, AZ5214 photoresist was spin coated under the same conditions and baked at 110 °C for 50 s followed by a dose of 40 mJ/cm<sup>2</sup>. The pattern used here was a 1 cm<sup>2</sup> array of circles with 20  $\mu\text{m}$  diameter and 35  $\mu\text{m}$  center to center distance. After exposure, the sample was baked at 115 °C for 2 min prior to a flood exposure with a dose of 240 mJ/cm<sup>2</sup>. The second bake and exposure enables image reversal of the mask pattern. After patterning, silicon pillars were formed by etching silicon using inductively coupled plasma (ICP) etching, Bosch process. We used an SF<sub>6</sub> flow rate of 100 sccm and a C<sub>4</sub>F<sub>8</sub> flow rate of 1 sccm under a plasma forward power of 700 W. Under this controlled condition, we repeated the process for 125 Bosch cycles and obtained the pillars with 25  $\mu\text{m}$  height. After this step, we immersed the silicon pillars in a stirred 30% potassium hydroxide (KOH) solution at 75 °C, which resulted in the desired tip shape.

Figure 2(a) shows the SEM image of initial silicon pillars after ICP, and Fig. 2(b) is an SEM image of the array of silicon tips. Importantly, we see the uniformity of this approach as evidenced through the SEM images. The side

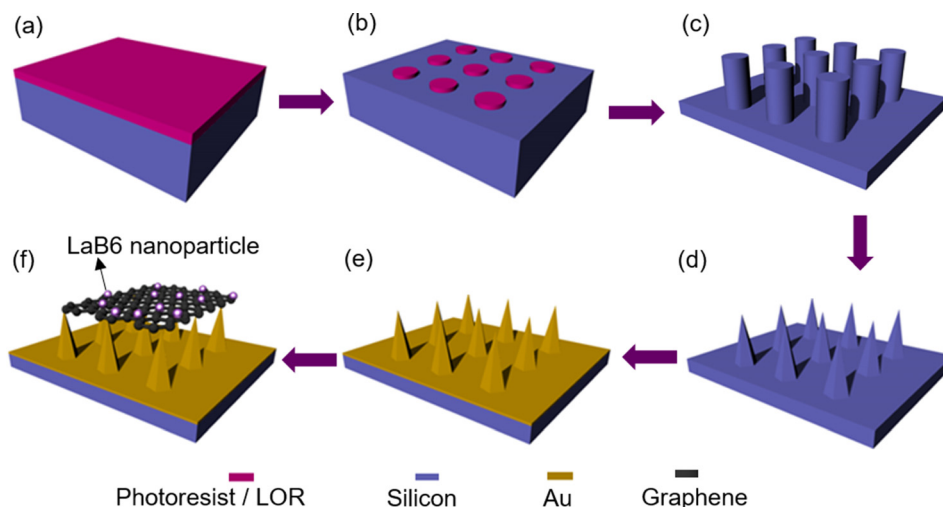


Fig. 1. (Color online) Fabrication procedure of hybrid emitter on sharp tip silicon arrays including (a) photoresist coating, (b) photolithography patterning, (c) silicon pillars formed through deep silicon etching (ICP process), (d) silicon pillars array immersed in KOH for anisotropic etching to sharpen the tip, (e) 10 nm thin layer of Au deposited on sharp tip silicon array, and (f) graphene transfer and  $\text{LaB}_6$  drop cast on sharp tip silicon array. Note that  $\text{LaB}_6$  nanoparticles are drop casted on graphene layer.

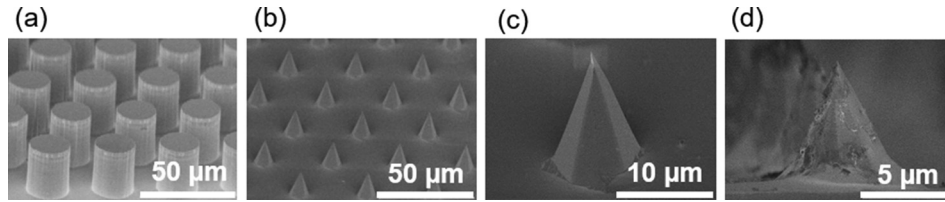


Fig. 2. SEM images of the fabrication steps for the sharp tip silicon array including (a) initial silicon pillars array, (b) sharp tip silicon array after anisotropic etching inside KOH, (c) cross section tilted view of single sharp tip silicon pillar, and (d) cross section view of a sharp tip silicon array after graphene sheet transfer and LaB<sub>6</sub> nanoparticles deposition.

view of the silicon tip is shown in Fig. 2(c) and allowed us to determine the exact geometry after processing. It should be noted that the height of pillars after etching is approximately 7 μm, as shown in Fig. 2(c). After fabricating the silicon tip array, we evaporated 10 nm of Au as an electrical contact. Next, we transferred graphene on the sharp tip array. The graphene used in our work was CVD grown graphene and we used wet transfer technique for transferring graphene on the sharp tip array. The graphene was characterized using Raman-spectroscopy as shown in Fig. 3(a) indicating that a sharp peak of the 2D band at 2689 cm<sup>-1</sup> corresponds to the second-order vibration caused by the scattering of phonons. We also observed the G band peak at 1580 cm<sup>-1</sup> which results from the E<sub>2g</sub> vibration mode of the sp<sup>2</sup> bonded carbon. There is a known correlation between the ratio of the Raman intensity of these two bands (I<sub>2D</sub>/I<sub>G</sub>) and the number of layers in the graphene sheet. It has been reported that the I<sub>2D</sub>/I<sub>G</sub> ratio decreases with the increase of layer numbers, where a value greater than 2.0 indicates the presence of monolayer graphene.<sup>25</sup> For the samples fabricated here, we measured an I<sub>2D</sub>/I<sub>G</sub> value of 2.5, indicating a successful transfer of monolayer graphene on the field emission device. After graphene transfer, we used low work function LaB<sub>6</sub> nanoparticles to reduce the work function on the surface. The LaB<sub>6</sub> nanoparticles used in this work was in deionized water solvent. An enhanced emission current had been measured from thin LaB<sub>6</sub> layer specifically layers thinner than 10 nm.<sup>26</sup> Therefore, the LaB<sub>6</sub> nanoparticles with an average size of 3–4 nm were synthesized using a previously reported method.<sup>27</sup> Briefly, 1.0 g anhydrous LaCl<sub>3</sub> (4.1 mmol) and 0.95 g NaBH<sub>4</sub> (25.1 mmol) were mixed under argon for 20 min and then heated to 360 °C at a rate of 10 °C/s. The reactants were stirred at 360 °C for 60 min and then cooled to room temperature. Work-up was performed in air, where MeOH was used to remove excess NaBH<sub>4</sub>, HCl to convert residual Na to NaCl, and deionized water was used to wash out the NaCl. Then, we made 1:10 dilution of nanoparticle solution and isopropyl alcohol and drop casted on the graphene sheet on a sharp tip array while leaving the sample under fume hood to allow evaporation of the solvent. The SEM image of the hybrid emitter after nanoparticle deposition is shown in Fig. 2(d).

### III. RESULTS AND DISCUSSION

This hybrid emitter of LaB<sub>6</sub> nanoparticles on the graphene sheet has a work function that is different from

pristine LaB<sub>6</sub> nanoparticles and graphene sheets. It is well known that the work function of a material is extremely sensitive to surface orientation, oxides, organic residues, etc. Thus, to accurately determine the field enhancement factor, the work function of the samples must be directly measured.

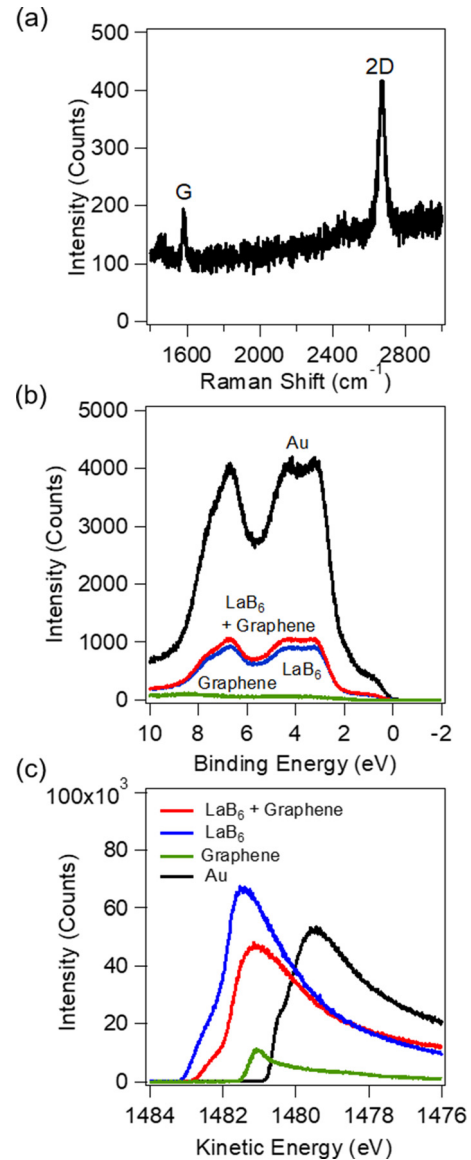


Fig. 3. (a) (Color online) Raman spectrum characteristic of the transferred graphene on sharp tip silicon array indicating monolayer graphene, (b) valence band spectrum of Au, graphene, LaB<sub>6</sub>, and hybrid emitter with the Fermi level ( $E_F$ ) at zero binding energy, and (c) secondary electron cutoff of the photoelectron spectrum.

To precisely determine the work function, we used a PES process<sup>28</sup> on the planar versions of our devices. The measured valence band spectrum with the Fermi level ( $E_F$ ) at zero binding energy and the secondary electron cutoff of the photoelectron spectrum is shown in Figs. 3(b) and 3(c), respectively. Based on this experimental data, we used the previously reported method<sup>28</sup> and measured the value of the effective work function for a  $\text{LaB}_6$  nanoparticle emitter on 10 nm Au is measured to be 3.3 eV, which is higher than the work function of the pristine bulk  $\text{LaB}_6$  and it is due to underlying Au contacts. Furthermore, the work function of the  $\text{LaB}_6$  nanoparticle on the graphene sheet on 10 nm Au is measured to be 3.62 eV, slightly higher than  $\text{LaB}_6$  nanoparticles on a 10 nm Au and significantly lower than the pristine graphene sheet. This measurement verifies that the graphene emitter work function can be reduced significantly at the surface using low work function nanoparticles. After fabrication of the devices and materials characterization, we carried out field emission measurements.

The field emission characteristics for each device were measured at room temperature under a vacuum of  $10^{-8}$  Torr. The current measurement was carried out using a Keithley 6485 picoammeter connected directly to our cathode, ensuring that all measured current was field emission, and no secondary electron emission current was measured. The field emitter device served as the lower electrode (cathode) and the high voltage (HV) top electrode (anode) made of stainless steel was positioned 1 mm above the cathode. The patterned area was  $1 \text{ cm}^2$  array of sharp tips. The distance was

measured using a linear motion feedthrough. Specifically, the anode was brought into electrical contact with a nonemitting area of the sample and then retracted by the amount desired for the anode–cathode separation. The high voltage was applied and swept using a Spellman high voltage source with a positive voltage. We measured the emission current from bare silicon, Si/Au, Si/graphene, Si/Au/ $\text{LaB}_6$ , and Si/Au/graphene/ $\text{LaB}_6$ , each in a planar and tip array configuration. We show the I-E curves in Figs. 4(a) and 4(b), and extracted the threshold field (defined as electric field required for  $J = 10 \mu\text{A}/\text{cm}^2$ ) as shown in Table I. We see that the bare silicon exhibits the highest threshold field of  $V_{\text{th}} = 12.5 \text{ V}/\mu\text{m}$  while the Si/Au/graphene/ $\text{LaB}_6$  hybrid on an array of silicon tips shows a much lower threshold field of  $V_{\text{th}} = 2.6 \text{ V}/\mu\text{m}$ . We also observed the highest current density from a hybrid Si/Au/graphene/ $\text{LaB}_6$  emitter at a higher field, higher than the Si/Au/ $\text{LaB}_6$  emitter. This is due to contribution of the graphene sheet to emission current which starts at a higher field compared to the  $\text{LaB}_6$  emitter. In addition, the threshold field for emitters on the silicon tip array is  $1.4 \times - 1.7 \times$ , smaller than the ones on planar (nonpatterned) silicon substrates due to engineered increase of the field enhancement factor. Specifically, the hybrid emitter on the silicon tip array has the lowest threshold field of  $V_{\text{th}} = 2.6 \text{ V}/\mu\text{m}$ , which is  $1.7 \times$  lower than the hybrid emitter on the planar substrate.

To analyze the results, Fowler–Nordheim theory was used to correlate the current density and local electric field to the geometrical and material properties of the fabricated

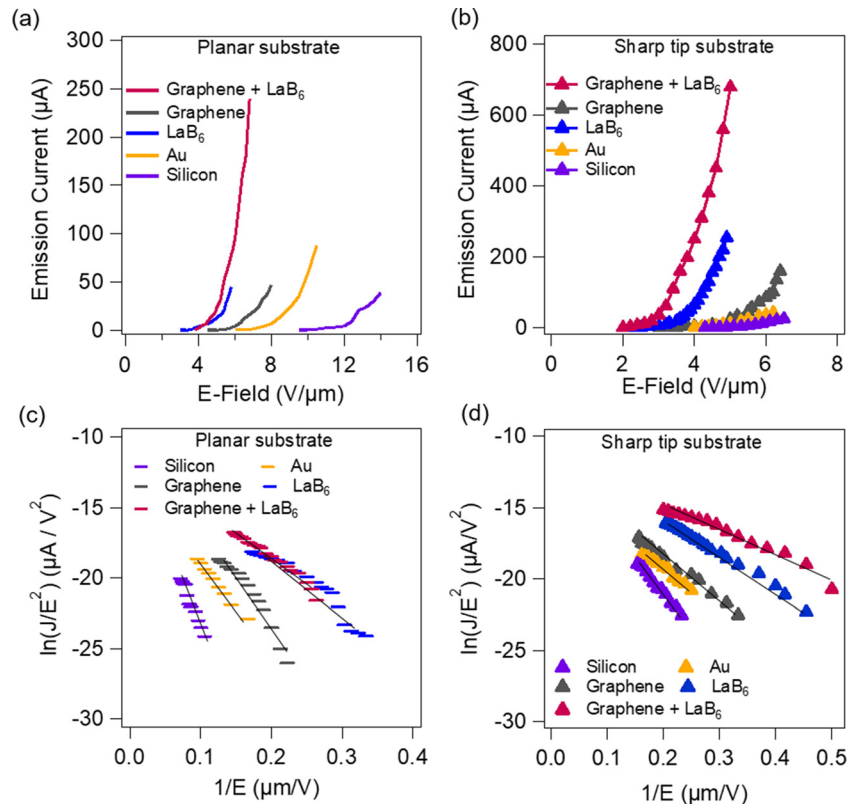


FIG. 4. (Color online) Emission characteristics of different emitter and corresponding FN plots: (a)–(c) on planar substrate and (b)–(d) on a sharp tip silicon array.

TABLE I. Threshold field  $V_{th}$  for  $J = 10 \mu\text{A}/\text{cm}^2$  and field enhancement factor.

	$V_{th}$ (V/ $\mu\text{m}$ ) for $J = 10 \mu\text{A}/\text{cm}^2$	Field enhancement factor $\beta$
Planar silicon	12.5	450
Silicon tip array	5.8	1217
Au on planar silicon	8.2	1275
Au on silicon tip array	4.9	2488
Graphene on planar silicon	6.4	904
Graphene on silicon tip array	4.5	2270
LaB <sub>6</sub> on planar silicon	4.8	1094
LaB <sub>6</sub> on silicon tip array	3.2	1716
LaB <sub>6</sub> on graphene on planar silicon	4.5	1285
LaB <sub>6</sub> on graphene on silicon tip array	2.6	2775

emitter. The FN theory of electron emission is encapsulated by the following equation:<sup>10,29</sup>

$$J = \left( \frac{A\beta^2 E^2}{\phi} \right) \exp \left( - \frac{B\phi^{3/2}}{\beta E} \right). \quad (1)$$

Here,  $A$  and  $B$  are constants equal to  $1.54 \times 10^{-6}$  A eV  $\text{V}^{-2}$  and  $6.83 \times 10^3$  eV $^{-3/2}$  V  $\mu\text{m}^{-1}$ , respectively.  $\beta$  is the field enhancement factor,  $E$  is the applied field calculated from the ratio of the applied voltage to the cathode–anode distance,  $J$  is the emission current density obtained from the total measured current divided by the area of the sharp tip silicon array, and  $\phi$  is the emitter work function. The field enhancement factor  $\beta$  can be calculated using the slope of the fitted straight line from a curve of  $\ln(J/E^2)$  versus  $1/E$  if the work function is known. Typically, the work function of the material and field enhancement factor are both treated as variables, utilizing the previously measured work function, such as 4.57 eV for graphene<sup>30</sup> and the work function measured using PES for the emitters which had the LaB<sub>6</sub> nanoparticles. After establishing the work function of our emitters, we can accurately calculate the field enhancement factor of these samples from the slope of the FN plots as shown in Figs. 4(c) and 4(d). The extracted field enhancement factors are tabulated in Table I.

The field enhancement factors from emitter on planar substrates are due to local protrusions within emitters that enhance the electric field as well as the nature of the constants in the FN equation. Specifically, those constants do not include material specific information, and are derived from certain assumptions. However, since we have measured all samples with both planar and tip array geometries, we can look at the relative change of the field enhancement factor with no loss of accuracy. It should be noted that the total electric field enhancement factor of hybrid emitters can be represented by<sup>31</sup>

$$\beta_{\text{overall}} = \beta_{\text{geometry}} \cdot \beta_{\text{emitter}}, \quad (2)$$

where,  $\beta_{\text{geometry}}$ ,  $\beta_{\text{emitter}}$  are the geometrical field enhancement factors from the silicon tip array, and field enhancement factor due to emitter material and surface roughness, respectively.

The value of  $\beta_{\text{emitter}}$  was obtained from the emitter on the planar silicon substrate and  $\beta_{\text{overall}}$  was also obtained from the hybrid emitter experimentally. Therefore, the value of the geometrical field enhancement,  $\beta_{\text{geometry}}$ , can be calculated. The obtained value of  $\beta_{\text{geometry}}$  for graphene is 2.51, for LaB<sub>6</sub> is 1.57, and for the hybrid emitter is 2.16. To validate the observed results, we used FINITE ELEMENT METHOD MAGNETICS software to calculate the expected geometrical field enhancement. The geometry of the silicon tip array was obtained from SEM images, including the geometry of the tip itself. The microfabricated tip has a spherical end with a diameter of 300 nm. In our simulation, 1000 V was applied to the HV electrode, which was separated by 1 mm from the silicon tip array. This configuration results in 1 V/ $\mu\text{m}$  uniform field in the case of a planar cathode; however as shown in Fig. 5, the electric field intensity is enhanced by  $6\times$  at a very small area of the spherical part of the silicon tip and  $2.5\times$  at a larger area of the lower level of the silicon tip. This result is in good agreement with the experimental observation.

As the graphene emitter should have the least surface roughness in the planar form, we expect it would give results most closely matching simulation, which is what is observed. However, the measured field enhancement factor value difference between the planar and tip array LaB<sub>6</sub> emitters is quite a bit lower. We believe that this discrepancy occurs due to the drop casting method of the LaB<sub>6</sub> particles on the planar silicon, where it is possible for aggregation to occur, which could cause deviations from the planar geometry assumed here. This drives up the field enhancement factor of the planar electrode, and reduces the difference with the silicon tip array.

Stability of the field emission current is another important parameter. The result of stability test for 6 hours is shown in Fig. 6 and indicates that there is no degradation throughout the stability test. We observed stable electron emission from the graphene emitter during the testing period. In addition, emission current from LaB<sub>6</sub> nanoparticle emitters shows small variation at the beginning before stabilizing. This longer time was required for LaB<sub>6</sub> nanoparticle to get rid of moisture and to desorb residual gas molecules after drop casting them on the emitter's surface. This trend of initial variation in emission current was observed and reported by others as well.<sup>32</sup>

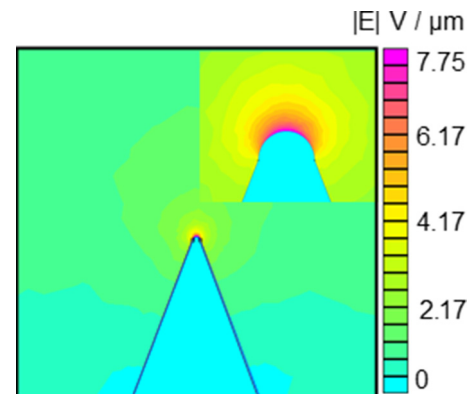


Fig. 5. (Color online) Simulated geometrical field enhancement.

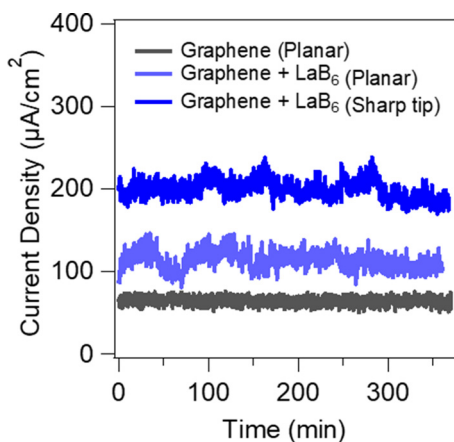


FIG. 6. (Color online) Emission current stability test.

#### IV. SUMMARY AND CONCLUSION

In conclusion, we report a technique for independent engineering the field enhancement and work function of a field emission device. Specifically, the silicon tip array enhances the local field intensity in the graphene emitter and the LaB<sub>6</sub> nanoparticles deposited on the surface of the graphene reduces the effective work function of the emitter. We have showed experimentally that these two techniques drastically improve the electron emission performance, reducing the threshold field by about 5×. We also performed simulations of the geometrical field enhancement factor to evaluate the contribution of the geometrical field enhancement and find excellent agreement with our experimental results. In the future, higher aspect ratio pillars can be easily made to improve the field enhancement factor from the present value of 2–4 as compared to planar to upward of 25, which would result in ultralow turn on voltages of  $V_{th} \sim 0.25$  V for these devices.

#### ACKNOWLEDGMENTS

This work was supported by AFOSR Grant No. FA9550-16-1-0306, NSF Award No. 1402906 (N.P.), and the Molecular Foundry at Lawrence Berkeley National Laboratory, a user facility supported by the Office of Science, Office of Basic Energy Sciences of the U.S. Department of Energy (DOE) under Contract No. DE-AC02-05CH11231.

<sup>1</sup>H. Sugie, M. Tanemura, V. Filip, K. Iwata, K. Takahashi, and F. Okuyama, *Appl. Phys. Lett.* **78**, 2578 (2001).

<sup>2</sup>C. Vieu, F. Carcenac, A. Pepin, Y. Chen, M. Mejias, A. Lebib, L. Manin-Ferlazzo, L. Couraud, and H. Launois, *Appl. Surf. Sci.* **164**, 111 (2000).

<sup>3</sup>C. A. Brau, *Free-Electron Lasers* (Academic, 1990).

<sup>4</sup>Q. H. Wang, A. A. Setlur, J. M. Lauerhaas, J. Y. Dai, E. W. Seelig, and R. P. H. Chang, *Appl. Phys. Lett.* **72**, 2912 (1998).

<sup>5</sup>A. Persaud, I. Allen, M. R. Dickinson, T. Schenkel, R. Kapadia, K. Takei, and A. Javey, *J. Vac. Sci. Technol., B* **29**, 02B107 (2011).

<sup>6</sup>A. Persaud, O. Waldmann, R. Kapadia, K. Takei, A. Javey, and T. Schenkel, *Rev. Sci. Instrum.* **83**, 02B312 (2012).

<sup>7</sup>J. Goldstein, D. E. Newbury, P. Echlin, D. C. Joy, A. D. Romig, Jr., C. E. Lyman, C. Fiori, and E. Lifshin, *Scanning Electron Microscopy and X-Ray Microanalysis: A Text for Biologists, Materials Scientists, and Geologists* (Springer, 2012).

<sup>8</sup>L. Reimer, *Transmission Electron Microscopy: Physics of Image Formation and Microanalysis* (Springer, 2013).

<sup>9</sup>J. H. Booske, R. J. Dobbs, C. D. Joye, C. L. Kory, G. R. Neil, G.-S. Park, J. Park, and R. J. Temkin, *IEEE Trans. Terahertz Sci. Technol.* **1**, 54 (2011).

<sup>10</sup>R. H. Fowler and L. Nordheim, paper presented at the Proceeding of Royal Society A: Mathematical, Physical and Engineering Sciences, 1928.

<sup>11</sup>F. Rezaeifar and R. Kapadia, *J. Vac. Sci. Technol., B* **34**, 041228 (2016).

<sup>12</sup>D. H. Dowell *et al.*, *Nucl. Instrum. Methods Phys. Res., Sect. A* **622**, 685 (2010).

<sup>13</sup>P. Avouris, *Nano Lett.* **10**, 4285 (2010).

<sup>14</sup>O. Waldmann, A. Persaud, R. Kapadia, K. Takei, F. I. Allen, A. Javey, and T. Schenkel, *Thin Solid Films* **534**, 466 (2013).

<sup>15</sup>A. Persaud, T. Schenkel, R. Kapadia, K. Takei, and A. Javey, paper presented at ICOPS, 2012.

<sup>16</sup>A. H. C. Neto, F. Guinea, N. M. R. Peres, K. S. Novoselov, and A. K. Geim, *Rev. Mod. Phys.* **81**, 109 (2009).

<sup>17</sup>S. Santandrea, F. Giubileo, V. Grossi, S. Santucci, M. Passacantando, T. Schroeder, G. Lupina, and A. Di Bartolomeo, *Appl. Phys. Lett.* **98**, 163109 (2011).

<sup>18</sup>G. Eda, H. E. Unalan, N. Rupesinghe, G. A. J. Amarantunga, and M. Chhowalla, *Appl. Phys. Lett.* **93**, 233502 (2008).

<sup>19</sup>Z. Pan *et al.*, *Adv. Mater.* **12**, 1186 (2000).

<sup>20</sup>C. J. Lee, T. J. Lee, S. C. Lyu, Y. Zhang, H. Ruh, and H. J. Lee, *Appl. Phys. Lett.* **81**, 3648 (2002).

<sup>21</sup>M. Dixon, *Activation Studies of Negative Electron Affinity Gallium Arsenide* (Cornell University, 2011), see [https://www.classe.cornell.edu/~ib38/reu/11/Dixon\\_report.pdf](https://www.classe.cornell.edu/~ib38/reu/11/Dixon_report.pdf).

<sup>22</sup>D. M. Goebel, Y. Hirooka, and T. A. Sketchley, *Rev. Sci. Instrum.* **56**, 1717 (1985).

<sup>23</sup>D. M. Goebel, R. M. Watkins, and K. K. Jameson, *J. Propul. Power* **23**, 552 (2007).

<sup>24</sup>D. Meeker, *FEMM* **4**, 32 (2010).

<sup>25</sup>F. Tuinstra and J. Lo Koenig, *J. Chem. Phys.* **53**, 1126 (1970).

<sup>26</sup>M. P. Kirley, B. Novakovic, N. Sule, M. J. Weber, I. Knezevic, and J. H. Booske, *J. Appl. Phys.* **111**, 063717 (2012).

<sup>27</sup>T. M. Mattox, A. Agrawal, and D. J. Milliron, *Chem. Mater.* **27**, 6620 (2015).

<sup>28</sup>R. Schlaf, *Calibration of Photoemission Spectra and Work Function Determination* (University of South Florida, 2014), see <http://rsl.eng.usf.edu/Documents/Tutorials/PEScalibration.pdf>.

<sup>29</sup>T. E. Stern, B. S. Gossling, and R. H. Fowler, *Proc. R. Soc. A* **124**, 699 (1929).

<sup>30</sup>Y.-J. Yu, Y. Zhao, S. Ryu, L. E. Brus, K. S. Kim, and P. Kim, *Nano Lett.* **9**, 3430 (2009).

<sup>31</sup>R. Miller, Y. Y. Lau, and J. H. Booske, *J. Appl. Phys.* **106**, 104903 (2009).

<sup>32</sup>D. J. Late, M. A. More, D. S. Joag, P. Misra, B. N. Singh, and L. M. Kukreja, *Appl. Phys. Lett.* **89**, 123510 (2006).